Available online at www.sciencedirect.com

Manufacturing Letters

Manufacturing Letters 00 (2026) 000–000

54th SME North American Manufacturing Research Conference (NAMRC 54, 2026)

Real-time In-situ Pyrometry and Emission Analytics in Laser Powder Bed Fusion

George Galkin[a,b], R. Sharma[a,b], Robert X. Gao[c], Y.B. Guo[a,b*]

[a] *Dept. of Mechanical and Aerospace Engineering, Rutgers University-New Brunswick, Piscataway, NJ 08854, USA*
[b] *New Jersey Advanced Manufacturing Institute, Rutgers University-New Brunswick, Piscataway, NJ 08854, USA*
[c] *Dept. of Mechanical and Aerospace Engineering, Case Western Reserve University, Cleveland, OH 44106, USA*

* Corresponding author. Tel.: +1-848-445-2225; fax: +1-732-445-3124. *E-mail address:* yuebin.guo@rutgers.edu

Abstract

Real-time process monitoring is the enabling tool for process stability for laser powder bed fusion. Massive noisy data are often ingested due to laser resetting, skywriting, and process dynamics in emerging monitoring techniques such as pyrometry. However, data curation of the big raw data imposes a daunting task for process analytics and data-driven models. This work develops a systematic and physics-guided curation workflow. Then, pyrometry analytics has been established to correlate process conditions (e.g., scanning vectors, energy density, and part orientation) and radiation intensity.

Peer-review under responsibility of the scientific committee of the NAMRI/SME.
Keywords: Pyrometry; Laser powder bed fusion; Process monitoring; Data analytics; Data curation

1. Introduction

Laser powder bed fusion (LPBF) processes are capable of producing metal and ceramic parts with complex and cavernous geometries. However, the extreme process dynamics (1) (e.g., severe temperature/pressure gradients, Marangoni flow) may cause an unstable printing process which leads to deteriorated printing quality, such as high surface roughness (2) random volumetric defects (e.g., pores, lack of fusion) (3), large tensile residual stresses (4), and heterogeneous microstructures (5). These quality variations (particularly volumetric defects) may affect part functionality (e.g., fatigue scattering (6)) by compromising the structural integrity or distorting the printed parts (7). In addition, random conditions such as the quality of the deposited powder layer powder and the presence of splatters mean that even under refined, stable, and highly controlled process conditions, part quality may still be affected. In precision manufacturing, guaranteeing part quality is paramount. The post-processing techniques, while preserving their integrity, present significant time and cost challenges. Conversely, the application of real-time in-situ monitoring methodologies, such as pyrometry and high-speed imaging, during the printing process offers a cost-effective, highly sensitive, and rapid data acquisition alternative. Therefore, there is a need to develop effective process monitoring methods that can identify defects reliably, quickly, and cheaply.

The high potential for improvement in LPBF process performance through in-situ process monitoring has attracted the attention of various research organizations and AM system developers. Many in-situ sensing techniques and principles have been investigated for their effectiveness in identifying process defects, including acoustics, pyrometry, optical imaging, infrared imaging, and pyrometric imaging. In general, in-situ monitoring techniques for LPBF monitoring can be placed into two categories: (i) co-axial monitoring of the point of production about the processing laser path and (ii) off-axial

Peer-review under responsibility of the scientific committee of the NAMRI/SME.

monitoring through lasers placed outside the laser path. Table 1 summarizes current in-situ monitoring methodologies used in LPBF. Most early studies focused on a single category of monitoring method, though recently, sensor-fusion techniques have been used to combine the readings of multiple sensors utilizing different monitoring methods.

Table 1: Key process monitoring techniques for LPBF

Principle	In/Ex-Situ	Defect/Property	Ref.
Ultrasonic	In/Ex-Situ	Porosity	(8-10)
Acoustic Emission	In-Situ	Spatter, Balling, Porosity, Undercut	(11-13)
Optical Imaging	In-Situ	Geometry	(14, 15)
X-ray Tomography	In/Ex-Situ	Porosity, Geometry, Lack-of-Fusion, Fatigue Life	(16-19)
Eddy Current	In-Situ	Geometry	(20, 21)
Infrared Imaging	In-Situ	Overheating, Porosity, Lack-of-Fusion	(22, 23)
Point Pyrometry	In-Situ	Overheating, Porosity, Lack-of-Fusion	(24, 25)

An LPBF process utilizes a laser to selectively melt areas of metal powders. A thin layer (e.g., 30-50 µm) of metal powders experiences extremely rapid heating and melting, followed by fusion, solidification, and contraction. These enormous thermal fluctuations (~103-104 K/s) create a unique thermal cycle along with unorthodox physical properties, defects, and process conditions compared to conventional manufacturing processes (26). The volatile nature of the process results in many disturbing phenomena like melt pool turbulences, plasma formation, weld fume generation, flying particles, and material evaporation. These underlying phenomena create high noise and uncertainty in measurements drawn directly from the melt pool. In addition, the LPBF process occurs in an atmospherically controlled chamber, surrounded by sensitive and precise machinery alongside a high-power laser. This process complexity requires measuring equipment to be placed far away from the point of melting and fusion, often outside the processing chamber. As a result, many in-situ monitoring techniques involve long-range or indirect measurements, which are usually done by cameras, microphones, or pyrometers.

The high potential for improving LPBF process stability through in-situ process monitoring has attracted a lot of attention. From many in-situ sensing techniques and principles that have been investigated over the years, pyrometry stands out as a uniquely suitable technology due to its high polling rate, which allows it to detect microsecond temporal behaviors, as well as its direct connection to the thermal history of the printing process. Unlike thermocouples, pyrometry allows the collection of thermal data without contacting the target and circumvents many potential issues inherent in traditional monitoring methods. A Pyrometer records the intensity of the thermal radiation produced by the melt pool within a radius around the laser spot, allowing an operator to monitor the thermal behavior of the process at the point of production from a distance. The direct relationship between the thermal behavior of the melt pool and process physics can potentially establish a relationship between the measured thermal emissions (pyrometry) and part quality (surface finish, volumetric defects, residual stresses, and microstructures). Mohr et al. (27) present an initial methodology for measuring emissivity in an LPBF system. Pavlov et al. (28) highlight that in situations involving single-channel pyrometry, the temperature readings are influenced by the average intensity detected by the infrared sensor, leading to a potential underestimation of the a temperature. Gutknecht et al. (29) observed that the recorded temperatures were lower than the melting point of the material and identified areas of potential overheating using co-axial two-color pyrometry during the LPBF process. Tempelman et al. (12) used pyrometry data in featurization and machine learning models to identify keyhole pore formation in their LPBF process. Vallab et al. (30) used the Single camera-based two wavelength imaging pyrometry data to train the regression model and predict the melt pool depth and average grain size.

However, few researchers in the existing literature attempt to identify or even mention the signal noise in pyrometry. The process volatility, as well as the high-dynamic nature of the measurements, can cause significant signal noise in pyrometry. Also, the nature of pyrometric process monitoring means that it is prone to several unique confounding factors, including the measurement of irrelevant data when the laser moves from one track to another and edge noise created due to skywriting (the process of increasing the length of scan vector to compensate the acceleration and deceleration of laser at starting and end of scanning) as shown in Fig. 1. However, the direct use of such noisy raw data imposes a severe problem for data analytics including any data-driven models (e.g., machine learning (ML) models). Furthermore, data curation of the big raw data imposes a daunting task considering the data size (on the level of 100 Gb) and acquisition frequency (100+ kHz).

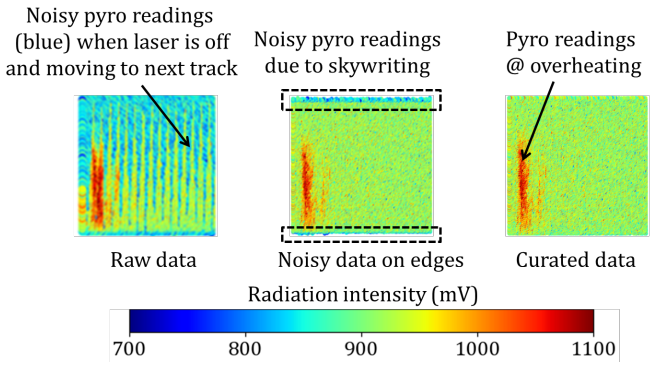

Fig. 1 Noisy pyrometer readings during an LPBF process.

In literature, many researchers use unprocessed raw data to ascertain melt pool temperatures, subsequently utilizing the flawed data for data analytics and ML model training, which yield misleading predictions and cover process insights. The objective of this work is four-fold: (1) assess how external factors impact the accuracy of pyrometric measurements, (2) create a systematic and physics-guided curation workflow to eliminate measurement noise, (3) understand the impact of different process parameters on pyrometry, and (4) assess the effectiveness of pyrometry to identify process anomaly.

2. Experimental Procedure

2.1. Measurement setup and sample preparation

The experiment used an AconityMINI LPBF printer configured with a fiber laser (up to 400W) and dual high-speed

pyrometers to apply multiple process parameters during one job. All parts were printed using a 30 μm layer thickness with an 80 μm diameter laser spot acting on stainless steel 316L powders. The particle size distribution is characterized by d10 = 18.00 μm, d50 = 29.66 μm, and d90 = 45.78 μm (measured using laser diffractometry). The experiments were conducted in an inert Argon atmosphere (O_2 < 200 ppm) with continuous recirculation to remove metal vapor, sparks, and condensate. The parts are printed on an SS 316L substrate, depicted as a grey circle in Fig. 2. The layout and part parametrizations are described as follows.

Table 2: LPBF process parameters.

Process parameters	Group A (part #)					Group B
	1, 6, 11	2, 7, 12	3, 8, 13	4, 9, 14	5, 10, 15	16-29
Scanning speed (mm/s)	800	900	1000	1100	1200	800
Power (W)	190	190	190	190	190	150
Hatch spacing (µm)	80	82.5	85	87.5	90	80
Energy density (J/mm^3)	98.96	85.3	74.51	65.8	58.64	78.13

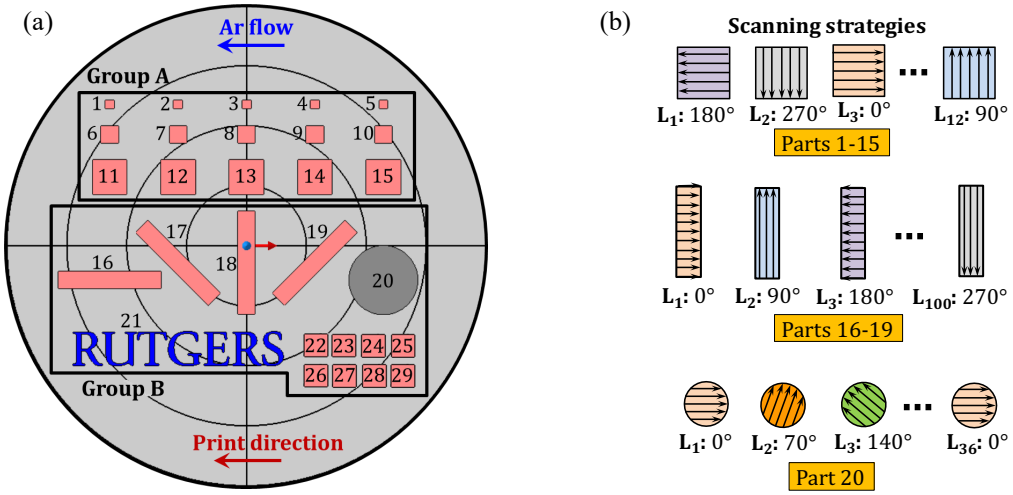

Fig. 2 (a) Printing layout, (b) Scanning strategies.

Group A (Parts 1-15) represents square samples with 2.5mm, 5mm, and 10mm scanning vector lengths for parts 1-5, 5-10, and 10-15, respectively, and 12 layers tall (360 μm) printed from right to left. These parts have parallel hatching vectors in the same direction which rotate 90 degrees CCW after each layer (Fig. 2b). This results in the top layer having parallel hatching vectors printed at 90° upwards with respect to the Argon flow. Each part uses a constant laser power (190W) but different laser speed and hatch spacing between individual vectors (Table 2). Each set of parameters was applied to every sample to examine the effect of vector length and part size on pyrometry across a wide set of process conditions. This setup can be used to examine the process behavior of different surface areas through pyrometry.

Group B (Parts 16-19) is a group of rectangular samples 5×30mm and 100 layers tall (3 mm). The scanning strategy also utilizes a 90-degree CCW rotation of hatching vectors, where the top layer's vectors are parallel with the long side and end at the bottom of the sample (right to left for part 16). This allows comparisons of theoretically identical pyrometry at various orientations on the build plate relative to the inert gas flow. The circular sample (Part 20) is also 100 layers tall, and each layer's hatching vectors rotate 70 degrees CCW starting horizontally against the argon flow (Fig. 2b). In this way, it provides scanning vectors at various angles before repeating itself after 36 layers. The circular cross-section allows the comparison of vectors of identical length and orientation at the start and end of each layer. The "RUTGERS" sample (Part 21) is 30 layers tall, uses the same scanning strategy as the samples 16-19, and can be used to evaluate the pyrometry of complex shapes. Parts 22-29 are single-layer calibration parts.

2.2. In-situ high-speed pyrometry

In-situ and real-time process monitoring was conducted with a 3D scanning device with two high-speed (100 kHz) co-axial pyrometers (31), which allows for the in-situ coaxial acquisition of the thermal radiation from the melt pool. The thermal emissions follow the laser's reverse path by first passing through the scanning device and beam expander before passing through the dichroic mirror and entering the process monitoring. This results in the collection of thermal emissions in a circular field of view with a ~400 µm diameter and a spatial accuracy within ±10 µm at the working surface. This ensures that thermal emissions from the entire melt pool are collected. Within the monitoring process, the emissions are split by an optical filter into two pyrometers. These individual pyrometers record the intensity of incoming radiation through a simple voltage output.

2.3. Pyrometry data processing

The thermal radiation data were measured in the 2000-2200 nm range at a 100 kHz acquisition frequency. The scanner and the pyrometers are configured to cover X and Y values (for each layer) in the range of -219 to 219 bits, covering an area of 400 × 400 mm, i.e., a calibration value of 1310.72 bit/mm. This theoretically allows the printer to be precise to within 0.382 μm. Considering the constant acquisition frequency of 100 kHz, a scanning speed of 1000 mm/s will produce measurements every 10 µm (similar calculations for other scanning speeds). A drawback of the constant acquisition speed

is that pyrometry measurements for parameter sets with lower scanning speeds are denser (i.e., the measurements are spaced closer together).

3. Data Analytics and Discussions

3.1. Understanding of pyrometry data

Understanding the nature and origin of the measured data sets is fundamental and critical to generating useful interpretations. In this case, the nature of the data collection fundamentally affects the data usability. The close-up image of the laser spot and recorded pyrometry data field at one instant of time is shown in Fig. 3a. A square of 400 µm side encapsulating 5 active vectors from part 11 is shown in Fig. 3b. Each small circle in Fig. 3b is located at the current position of the laser center, and represents the total intensity recorded by the pyrometer at that time instant. Each scanning vector moves upwards and starts at a point a little outside and below the square (skywriting). The dense vectors of the "hotter" point cloud (higher pyrometry readings) represent the data gathered by the pyrometer while the laser is active and melting powders across the surface, while the less dense vectors of the "cooler" point cloud represent data gathered by the pyrometer as the inactive laser spot moves from the end of the previous vector to the beginning of the adjacent vector. The laser spot moves faster during resetting (i.e., laser switching scan tracks) while the data acquisition frequency is fixed. Therefore, the "cooler" point cloud appears less dense. It is noteworthy to mention that certain positions lack data points, which is attributable to the fact that the pyrometer fails to capture data occasionally due to unidentified random factors, resulting in the omission of specific spots while recording pyrometer data. The affected areas are sufficiently small not to impact the macroscopic layer pyrometry measurements. Also, the recorded intensity of radiation is not uniform not because of overheating but due to signal attenuation because of the high-speed nature of the measurements, plasma formation, fume generation, flying particles, and material evaporation. The combination of the two factors - the high level of signal noise and the ambiguous nature of the data requires a unique data analytics algorithm to curate the measured raw data. In the following sections of the paper, the results are shown by removing the signal noise due to laser off while it switches between different tracks and skywriting.

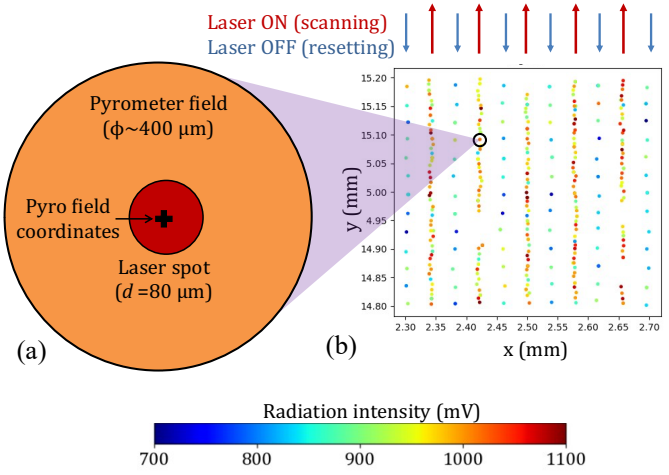

Fig. 3. (a) Pyrometer field, (b) Close-up of pyrometry data.

3.2. Pyrometry data curation and analytics

In this study, all raw data was curated using an in-house Python script. The script utilizes three filters to remove the noisy data (shown in Fig. 4). Step 1: the out-of-domain readings are rejected as the pyrometer keeps collecting data even when the laser moves from one location to another while depositing a new layer. Step 2: the noisy data recorded when the laser switches between different scanning tracks (i.e., resetting) are removed by utilizing the fact that the instantaneous laser moving speed is higher in resetting than the actual scanning. Step 3: the script removes the noisy data in the edge zones due to skywriting by comparing the edge emission values with the average emission value in the actual scanning area. Step 4: the script saves all curated data for subsequent pyrometry analytics.

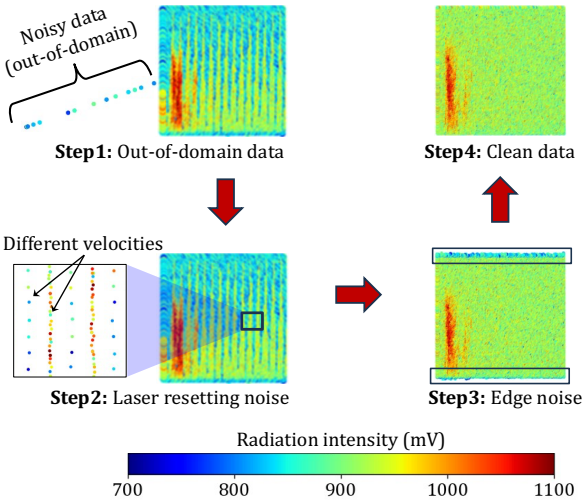

Fig. 4. Data curation steps.

Fig. 5 shows the pyrometry analytics for the top layer of samples in Group A with noisy data filtered out. The mean and standard deviation of thermal emission for the top layer are reported. These samples allow the analysis of vector lengths on different scanning areas at different volume energy densities. Excluding the three outliers (due to overheating) in the 10×10 mm part (parts 12-14), the average radiation intensity decreases with decreasing energy density (left to right). Also, increasing the scanning vector length (top to bottom) generates lower radiation intensity readings due to more heat dissipation because of the increased surface area. Notably, there are three outliers (i.e., overheating) in parts 12-14, where the average intensities seem highly inflated compared to part 11 (printed at a higher energy density). Overheating can be caused by the strong printing dynamics due to process uncertainties such as the random fluctuation of Argon flow during the printing process. The radiation map shows that overheating can be real-time monitored by online pyrometers. Overheating may also happen on the edge zones due to acceleration and deceleration of the laser, which may cause heat accumulation. Edge overheating can be avoided by using skywriting, where the laser travels more distance than the vector length to avoid acceleration and deceleration on the actual track. It covers the extra distance by turning off the scanning.

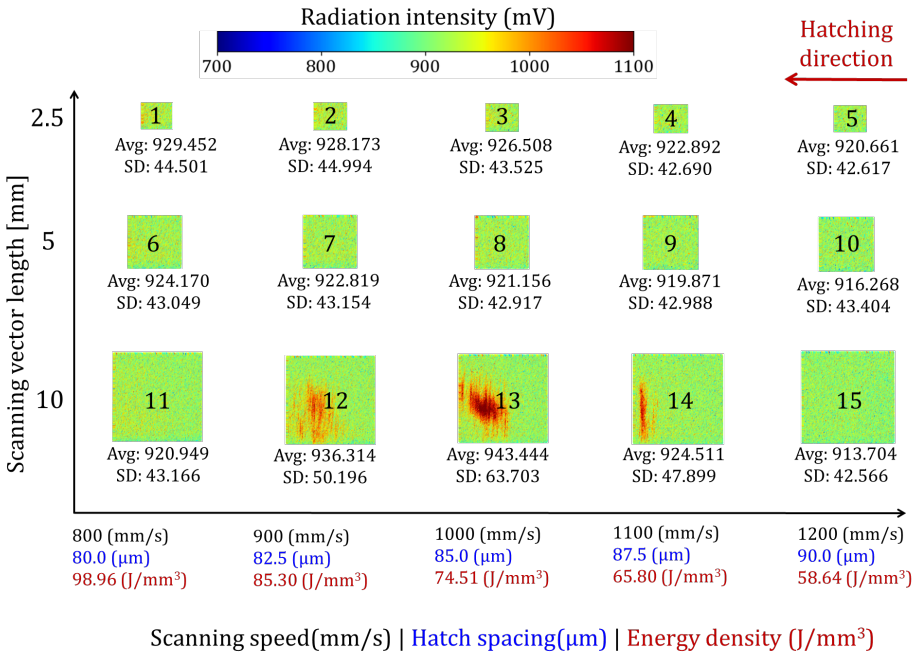

Fig. 5. Pyrometry analytics for samples in Group A.

Fig. 6 shows the time-series pyrometer data for Part 13 in normal and overheated areas (see Fig. 5). A low level of radiation intensity is recorded by the pyrometer when the laser moves from one part to another (Fig. 6a). During normal operations, a symmetric sinusoidal curve is obtained where the peak represents the radiation intensity value during the actual scanning. The valley represents the laser resetting operation (i.e., power off) when the laser moves from one track to another. Notably, in the overheated areas (Fig. 6b), the inactive vectors registered extremely high readings, even higher than actual scanning readings in normal operations. This implies that the residual heat from the overheated scanning is so high that the part surface is hotter than the normal conditions for several moments, even after the laser is turned off.

Fig. 7a shows four samples printed with identical process parameters, geometries, and hatching patterns, except for their initial orientations relative to the Argon flow direction. It can be observed that the parts have very similar intensity values with a slight decrease in average intensity values while moving from left to right. This could be due to the direction of Argon flow (right to left), which helps with quick heat dissipation in the areas near the Argon vent. Fig. 7b shows the average intensity of different layers for each part at different vector hatch angles. This means that each part contains four different types of scanning vectors. Two of these four vectors are long, and two are short. In Fig. 7b, each data point corresponding to a particular part represents the average intensity of one layer. The data point of each part lies under four different angles corresponding to its vector hatch angle. Hence, 25 data points corresponding to the specific hatch angle of a part are grouped into two categories – long and short - according to the vector length. It is observed that the long vectors have higher radiation intensities (also temperatures) than those of the short ones at the same angles. It is worth noting that part 18 (perpendicular to argon flow) shows the highest average intensity when scanning from top to down (270°), while part 16 shows the

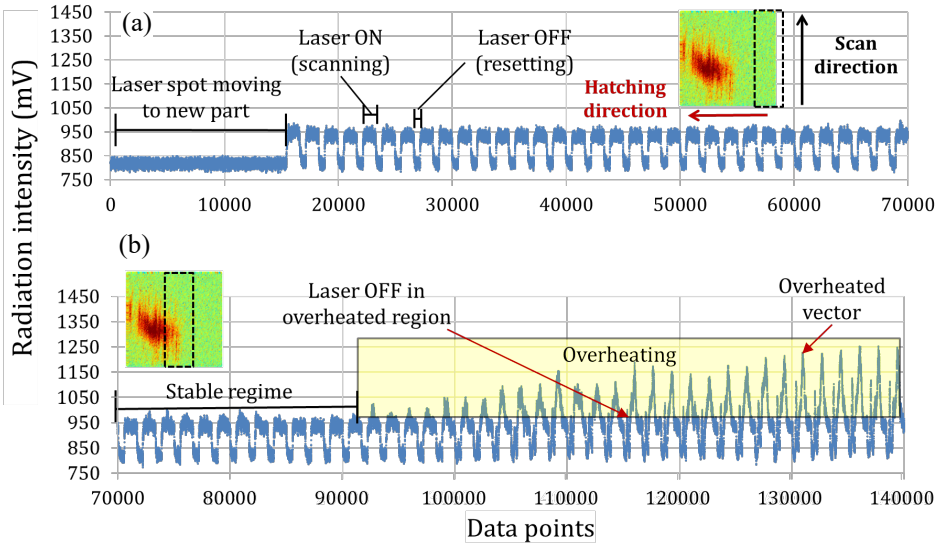

Fig. 6. Time-series data in (a) normal operations, (b) overheated region.

minimum combined average intensity for two different long vectors. It is recommended to print long vectors along the inert gas flow rather than perpendicular to it.

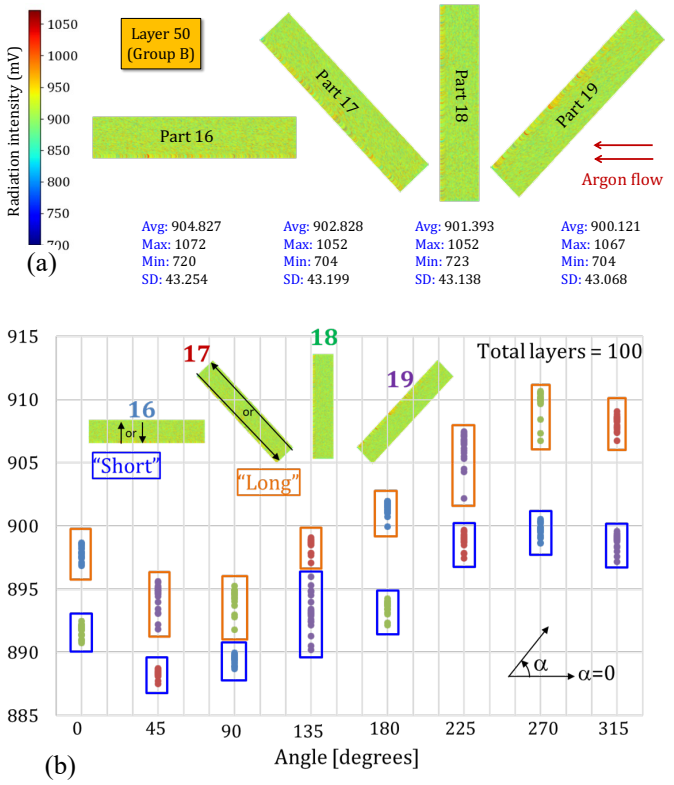

Fig. 7. (a) Irradiation intensities at different part orientations, (b) Average intensity vs. hatching angle for the rectangular parts.

For the cylindrical sample (Part 20), all the layers have the same vector length irrespective of orientation. This means that every layer has short and long vectors of the same size, regardless of the vectors' orientation. Therefore, Fig. 8 helps to understand the effect of inert gas flow on the intensity of radiation. Here, each data point represents the average intensity of one layer at the given hatch angle. It can be inferred that printing the part against the inert gas flow (α=180°) is more likely to cause overheating compared to printing along the flow (α=0° or 360°) when the vectors have the same length in each layer.

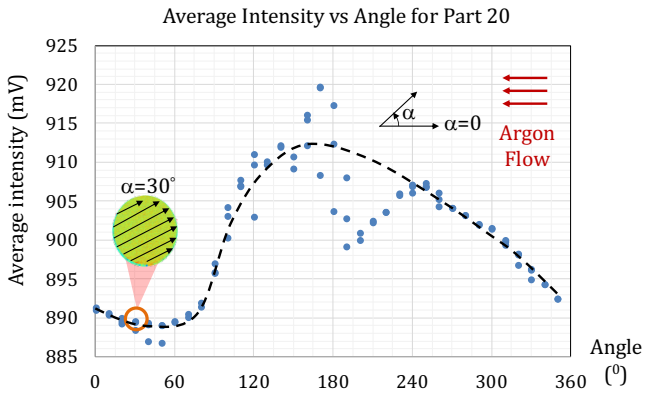

Fig. 8. Average intensity vs. hatching angle for the cylindrical part.

4. Conclusions

This work addresses the issue of noisy big data of high-speed co-axial pyrometry in LPBF and demonstrates the data cleaning methodology. Subsequently, it uses this data to understand the impact of different process parameters on pyrometry. Key results may be summarized as follows:

- The root cause of noisy pyrometry data is attributed to confounding factors, including laser resetting, skywriting, and process interference.
- Python script can be used as an effective method to curate the big data for pyrometry analytics.
- Long scanning vectors in printing large cube samples generate low radiation intensity because of more heat dissipation from the increasing surface area, while for the rectangular samples (same surface area), long scanning vectors generate high emissions compared to the shorter ones. Furthermore, the radiation intensity decreases with decreasing volumetric energy density.
- Overheating, either at the edge zone or inside a part, can be captured in real-time by the high-speed co-axial pyrometers.
- It is recommended to align long vectors printing parallel to the Argon flow rather than perpendicular to it.

In the future, emissivity data can be utilized to determine the actual temperature of the melt pool. The correlation between process conditions and emissivity lays a strong foundation for developing data-driven models and implementing online, model-based process control. Furthermore, these data-driven models enable the establishment of correlations between pyrometric readings and a wide array of material characteristics, including microstructure and residual stresses.

Acknowledgments

The authors would like to thank the financial support of the National Science Foundation under the grant CMMI-2323083.

References

[1] Yeung H, Yang Z, Yan L. A meltpool prediction based scan strategy for powder bed fusion additive manufacturing. Additive Manufacturing. 2020;35:101383.

[2] Levy GN, Schindel R, Kruth JP. Rapid Manufacturing And Rapid Tooling With Layer Manufacturing (Lm) Technologies, State Of The Art And Future Perspectives. CIRP Annals. 2003;52(2):589-609.

[3] Lewis GK, Schlienger E. Practical considerations and capabilities for laser assisted direct metal deposition. Materials & Design. 2000;21(4):417-23.

[4] Kruth JP, Froyen L, Van Vaerenbergh J, Mercelis P, Rombouts M, Lauwers B. Selective laser melting of iron-based powder. Journal of Materials Processing Technology. 2004;149(1):616-22.

[5] Wang YM, Voisin T, McKeown JT, Ye J, Calta NP, Li Z, et al. Additively manufactured hierarchical stainless steels with high strength and ductility. Nature Materials. 2018;17(1):63-71.

[6] Murakami Y, Takagi T, Wada K, Matsunaga H. Essential structure of S-N curve: Prediction of fatigue life and fatigue limit of defective materials and nature of scatter. International Journal of Fatigue. 2021;146:106138.

[7] Tammas-Williams S, Zhao H, Léonard F, Derguti F, Todd I, Prangnell PB. XCT analysis of the influence of melt strategies on defect population in Ti–6Al–4V components manufactured by Selective Electron Beam Melting. Materials Characterization. 2015;102:47-61.

[8] Honarvar F, Varvani-Farahani A. A review of ultrasonic testing applications in additive manufacturing: Defect evaluation, material characterization, and process control. Ultrasonics. 2020;108:106227.
[9] Allam A, Sugino C, Harding M, Bishop DP, Erturk A, Ruzzene M. Phased Array Ultrasonic Testing of Inconel 625 Produced by Selective Laser Melting. Journal of Nondestructive Evaluation, Diagnostics and Prognostics of Engineering Systems. 2021;4(4):041006.
[10] Sealy M, Hadidi H, Sotelo L, Li W, Turner J, McGeough J. Compressive behavior of 420 stainless steel after asynchronous laser processing. CIRP Annals. 2020;69(1):169-72.
[11] Drissi-Daoudi R, Masinelli G, de Formanoir C, Wasmer K, Jhabvala J, Logé RE. Acoustic emission for the prediction of processing regimes in laser powder bed fusion, and the generation of processing maps. Additive Manufacturing. 2023;67:103484.
[12] Tempelman JR, Wachtor AJ, Flynn EB, Depond PJ, Forien J-B, Guss GM, et al. Sensor fusion of pyrometry and acoustic measurements for localized keyhole pore identification in laser powder bed fusion. Journal of Materials Processing Technology. 2022;308:117656.
[13] Zhirnov I, Kouprianoff D, editors. Acoustic diagnostic of laser powder bed fusion processes. 10th Swedish Production Symposium, Skövde, Sweden, April 26-29, 2022; 2022: IOS Press.
[14] Guerra MG, Lafirenza M, Errico V, Angelastro A. In-process dimensional and geometrical characterization of laser-powder bed fusion lattice structures through high-resolution optical tomography. Optics & Laser Technology. 2023;162:109252.
[15] Ranjan R, Chen Z, Ayas C, Langelaar M, Van Keulen F. Overheating control in additive manufacturing using a 3D topology optimization method and experimental validation. Additive Manufacturing. 2023;61:103339.
[16] Yang J, Zhu Q, Wang Z, Xiong F, Li Q, Yang F, et al. Effects of metallurgical defects on magnetic properties of SLM NiFeMo permalloy. Materials Characterization. 2023;197:112672.
[17] Luo Z, Li D, Ojha A, Lai W-J, Engler-Pinto C, Li Z, et al. Prediction of high cycle fatigue strength for additive manufactured metals by defects incorporated crystal plasticity modeling. Materials Science and Engineering: A. 2023;870:144832.
[18] Barricelli L, Patriarca L, Du Plessis A, Beretta S. Orientation-dependent fatigue assessment of Ti6Al4V manufactured by L-PBF: Size of surface features and shielding effect. International Journal of Fatigue. 2023;168:107401.
[19] Du Plessis A, Yadroitsev I, Yadroitsava I, Le Roux SG. X-ray microcomputed tomography in additive manufacturing: a review of the current technology and applications. 3D Printing and Additive Manufacturing. 2018;5(3):227-47.
[20] Kasa T, Sun W, Hatsukade Y, Yonehara M, Ikeshoji T-T, Kyogoku H. Eddy Current Testing Based Non-Destructive Inspection for Metal 3D Additive Manufacturing Objects With HTS-SQUID. IEEE Transactions on Applied Superconductivity. 2023;33(5):1-4.
[21] Ehlers H, Pelkner M, Thewes R. Online process monitoring for additive manufacturing using eddy current testing with magnetoresistive sensor arrays. IEEE Sensors Journal. 2022;22(20):19293-300.
[22] Zhang H, Vallabh CKP, Zhao X. Registration and fusion of large-scale melt pool temperature and morphology monitoring data demonstrated for surface topography prediction in LPBF. Additive Manufacturing. 2022;58:103075.
[23] Estalaki SM, Lough CS, Landers RG, Kinzel EC, Luo T. Predicting defects in laser powder bed fusion using in-situ thermal imaging data and machine learning. Additive Manufacturing. 2022;58:103008.
[24] Vallabh CKP, Sridar S, Xiong W, Zhao X. Predicting melt pool depth and grain length using multiple signatures from in-situ single camera two-wavelength imaging pyrometry for laser powder bed fusion. Journal of Materials Processing Technology. 2022;308:117724.
[25] Terrazas-Nájera CA, Romero A, Felice R, Wicker R. Multi-wavelength pyrometry as an in situ diagnostic tool in metal additive manufacturing: Detecting sintering and liquid phase transitions in electron beam powder bed fusion. Additive Manufacturing. 2023;63:103404.
[26] Sharma R, Guo YB. Computational Modeling and Physics-Informed Machine Learning of Metal Additive Manufacturing: State-of-the-Art and Future Perspective. Annual Review of Heat Transfer. 2021;24.
[27] Mohr G, Nowakowski S, Altenburg SJ, Maierhofer C, Hilgenberg K. Experimental determination of the emissivity of powder layers and bulk material in laser powder bed fusion using infrared thermography and thermocouples. Metals. 2020;10(11):1546.
[28] Pavlov M, Doubenskaia M, Smurov I. Pyrometric analysis of thermal processes in SLM technology. Physics Procedia. 2010;5:523-31.
[29] Gutknecht K, Cloots M, Sommerhuber R, Wegener K. Mutual comparison of acoustic, pyrometric and thermographic laser powder bed fusion monitoring. Materials & Design. 2021;210:110036.
[30] Vallabh CKP, Sridar S, Xiong W, Zhao X. Predicting melt pool depth and grain length using multiple signatures from in-situ single camera two-wavelength imaging pyrometry for laser powder bed fusion. Journal of Materials Processing Technology. 2022;308.
[31] Galkin G, Gawade V, Guo W, Yi J, Guo YB. In-Situ and Real-Time 3D Pyrometry for Thermal History Diagnosis in Laser Fusion Process. Manufacturing Letters. 2022;33:862-71.